

The kaobook class

Use this document as a template

My PhD Thesis

Customise this page according to your needs

Tobias Hangleiter*

May 8, 2025

* A \LaTeX lover/hater

The harmony of the world is made manifest in Form and Number, and the heart and soul and all the poetry of Natural Philosophy are embodied in the concept of mathematical beauty.

– D'Arcy Wentworth Thompson

Contents

Contents	iii
I A FLEXIBLE PYTHON TOOL FOR FOURIER-TRANSFORM NOISE SPECTROSCOPY	1
1 Introduction	2
2 Theory of spectral noise estimation	4
2.1 Spectrum estimation from time series	5
2.2 Window functions	8
2.3 Welch's method	9
2.4 Parameters & Properties of the PSD	9
3 The <code>python_spectrometer</code> software package	11
3.1 Package design and implementation	11
3.1.1 Data acquisition	11
3.1.2 Data processing	13
3.2 Feature overview	14
3.2.1 Serial spectrum acquisition	15
3.2.2 Live spectrum acquisition	18
4 Conclusion and outlook	20
II CHARACTERIZATION AND IMPROVEMENTS OF A MILLIKELVIN CONFOCAL MICROSCOPE	23
5 Introduction	24
6 Characterization of electrical performance	25
6.1 Electron temperature	25
7 Characterization and improvements of the optical path	27
8 Vibration performance	28
8.1 Vibration isolation	28
8.2 Accelerometric vibration spectroscopy	30
8.3 Optical vibration spectroscopy	31
8.3.1 Noise floor	34
8.4 Routes for improvement	36
9 Conclusion & outlook	37
III OPTICAL MEASUREMENTS OF ELECTROSTATIC EXCITON TRAPS IN SEMICONDUCTOR MEMBRANES	38
IV A FILTER-FUNCTION FORMALISM FOR UNITAL QUANTUM OPERATIONS	39

APPENDIX	40
A Additional vibration spectroscopy data	41
Bibliography	42
List of Terms	44

List of Figures

2.1	Generated by <code>img/tikz/spectrometer/lockin_dut.tex</code>	4
2.2	Generated by <code>img/py/spectrometer/lorentz.py</code>	6
2.3	Generated by <code>img/py/spectrometer/pyspeck.py</code>	8
2.4	Generated by <code>img/py/spectrometer/pyspeck.py</code>	8
2.5	Generated by <code>img/py/spectrometer/pyspeck.py</code>	9
2.6	Generated by <code>img/tikz/spectrometer/daq_settings.tex</code>	10
3.1	Generated by <code>img/tikz/spectrometer/speck_tree.tex</code>	11
3.2	Generated by <code>img/py/spectrometer/pyspeck_workflow.py</code>	15
3.3	Generated by <code>img/py/spectrometer/pyspeck_workflow.py</code>	16
3.4	Generated by <code>img/py/spectrometer/pyspeck_workflow.py</code>	17
3.5	Generated by <code>img/py/spectrometer/pyspeck_workflow.py</code>	17
3.6	Generated by <code>img/py/spectrometer/pyspeck_workflow.py</code>	17
3.7	Generated by <code>img/py/spectrometer/pyspeck_workflow.py</code>	18
3.8	Generated by <code>img/py/spectrometer/pyspeck_live_view.py</code>	19
6.1	Generated by <code>img/py/setup/transport.py</code>	26
6.2	Generated by <code>img/py/setup/transport.py</code>	26
6.3	Generated by <code>img/py/setup/transport.py</code>	26
8.1	Generated by <code>img/pdf/setup/springs.py</code>	29
8.2	Generated by <code>img/py/setup/vibration_spectroscopy.py</code>	31
8.3	Generated by <code>img/tikz/setup/knife_edge.tex</code>	32
8.4	Generated by <code>img/py/setup/vibration_spectroscopy.py</code>	32
8.5	Generated by <code>img/py/setup/vibration_spectroscopy.py</code>	33
8.6	Generated by <code>img/py/setup/vibration_spectroscopy.py</code>	33
8.7	Generated by <code>img/py/setup/vibration_spectroscopy.py</code>	34

Publications

- [1] Yaiza Aragonés-Soria, René Otten, Tobias Hangleiter, Pascal Cerfontaine, and David Gross. “Minimising Statistical Errors in Calibration of Quantum-Gate Sets.” June 7, 2022. DOI: [10.48550/arXiv.2206.03417](https://doi.org/10.48550/arXiv.2206.03417). (Visited on 06/08/2022). Pre-published.
- [2] Pascal Cerfontaine, Tobias Hangleiter, and Hendrik Bluhm. “Filter Functions for Quantum Processes under Correlated Noise.” In: *Phys. Rev. Lett.* 127.17 (Oct. 18, 2021), p. 170403. DOI: [10.1103/PhysRevLett.127.170403](https://doi.org/10.1103/PhysRevLett.127.170403).
- [3] Thomas Descamps, Feng Liu, Sebastian Kindel, René Otten, Tobias Hangleiter, Chao Zhao, Mihail Ion Lepsa, Julian Ritzmann, Arne Ludwig, Andreas D. Wieck, Beata E. Kardynał, and Hendrik Bluhm. “Semiconductor Membranes for Electrostatic Exciton Trapping in Optically Addressable Quantum Transport Devices.” In: *Phys. Rev. Appl.* 19.4 (Apr. 28, 2023), p. 044095. DOI: [10.1103/PhysRevApplied.19.044095](https://doi.org/10.1103/PhysRevApplied.19.044095). (Visited on 04/28/2023).
- [4] Thomas Descamps, Feng Liu, Tobias Hangleiter, Sebastian Kindel, Beata E. Kardynał, and Hendrik Bluhm. “Millikelvin Confocal Microscope with Free-Space Access and High-Frequency Electrical Control.” In: *Review of Scientific Instruments* 95.8 (Aug. 9, 2024), p. 083706. DOI: [10.1063/5.0200889](https://doi.org/10.1063/5.0200889). (Visited on 08/12/2024).
- [5] Denny Dütz, Sebastian Kock, Tobias Hangleiter, and Hendrik Bluhm. “Distributed Bragg Reflectors for Thermal Isolation of Semiconductor Spin Qubits.”
- [6] Sarah Fleitmann, Fabian Hader, Jan Vogelbruch, Simon Humpohl, Tobias Hangleiter, Stefanie Meyer, and Stefan van Waasen. “Noise Reduction Methods for Charge Stability Diagrams of Double Quantum Dots.” In: *IEEE Trans. Quantum Eng.* 3 (2022), pp. 1–19. DOI: [10.1109/TQE.2022.3165968](https://doi.org/10.1109/TQE.2022.3165968).
- [7] Fabian Hader, Jan Vogelbruch, Simon Humpohl, Tobias Hangleiter, Chimezie Eguzo, Stefan Heinen, Stefanie Meyer, and Stefan van Waasen. “On Noise-Sensitive Automatic Tuning of Gate-Defined Sensor Dots.” In: *IEEE Trans. Quantum Eng.* 4 (2023), pp. 1–18. DOI: [10.1109/TQE.2023.3255743](https://doi.org/10.1109/TQE.2023.3255743).
- [8] Tobias Hangleiter, Pascal Cerfontaine, and Hendrik Bluhm. “Filter-Function Formalism and Software Package to Compute Quantum Processes of Gate Sequences for Classical Non-Markovian Noise.” In: *Phys. Rev. Research* 3.4 (Oct. 18, 2021), p. 043047. DOI: [10.1103/PhysRevResearch.3.043047](https://doi.org/10.1103/PhysRevResearch.3.043047). (Visited on 01/19/2022).
- [9] Tobias Hangleiter, Pascal Cerfontaine, and Hendrik Bluhm. “Erratum: Filter-function Formalism and Software Package to Compute Quantum Processes of Gate Sequences for Classical Non-Markovian Noise [Phys. Rev. Research 3, 043047 (2021)].” In: *Phys. Rev. Res.* 6.4 (Oct. 16, 2024), p. 049001. DOI: [10.1103/PhysRevResearch.6.049001](https://doi.org/10.1103/PhysRevResearch.6.049001). (Visited on 10/16/2024).
- [10] Isabel Nha Minh Le, Julian D. Teske, Tobias Hangleiter, Pascal Cerfontaine, and Hendrik Bluhm. “Analytic Filter-Function Derivatives for Quantum Optimal Control.” In: *Phys. Rev. Applied* 17.2 (Feb. 2, 2022), p. 024006. DOI: [10.1103/PhysRevApplied.17.024006](https://doi.org/10.1103/PhysRevApplied.17.024006). (Visited on 02/03/2022).
- [11] Paul Surrey, Julian D Teske, Tobias Hangleiter, Pascal Cerfontaine, and Hendrik Bluhm. “Data-Driven Qubit Characterization and Optimal Control Using Deep Learning.”
- [12] Kui Wu, Sebastian Kindel, Thomas Descamps, Tobias Hangleiter, Jan Christoph Müller, Rebecca Rodrigo, Florian Merget, Beata E. Kardynał, Hendrik Bluhm, and Jeremy Witzens. “Modeling an Efficient Singlet-Triplet-Spin-Qubit-to-Photon Interface Assisted by a Photonic Crystal Cavity.” In: *Phys. Rev. Appl.* 21.5 (May 24, 2024), p. 054052. DOI: [10.1103/PhysRevApplied.21.054052](https://doi.org/10.1103/PhysRevApplied.21.054052). (Visited on 08/21/2024).

Software

The following open-source software packages were developed (at least partially) during the work on this thesis.

- [1] Tobias Hangleiter, Isabel Nha Minh Le, and Julian D. Teske, *Filter_functions* version v1.1.3, May 14, 2024. Zenodo. doi: [10.5281/ZENODO.4575000](https://doi.org/10.5281/ZENODO.4575000).
- [2] Tobias Hangleiter, *Lindblad_mc_tools*.
- [3] Tobias Hangleiter, *Mjolnir*.
- [4] Tobias Hangleiter, Simon Humpohl, Max Beer, and René Otten, *Python-Spectrometer* version 2024.11.1, Nov. 21, 2024. Zenodo. doi: [10.5281/ZENODO.13789861](https://doi.org/10.5281/ZENODO.13789861).
- [5] Tobias Hangleiter, Simon Humpohl, Paul Surrey, and Han Na We, *Qutil* version 2024.11.1, Nov. 21, 2024. Zenodo. doi: [10.5281/ZENODO.14200303](https://doi.org/10.5281/ZENODO.14200303).

Part I

**A FLEXIBLE PYTHON TOOL FOR
FOURIER-TRANSFORM NOISE
SPECTROSCOPY**

Part II

CHARACTERIZATION AND IMPROVEMENTS OF A MILLIKELVIN CONFOCAL MICROSCOPE

Introduction

5



Characterization of electrical performance

6



6.1 Electron temperature

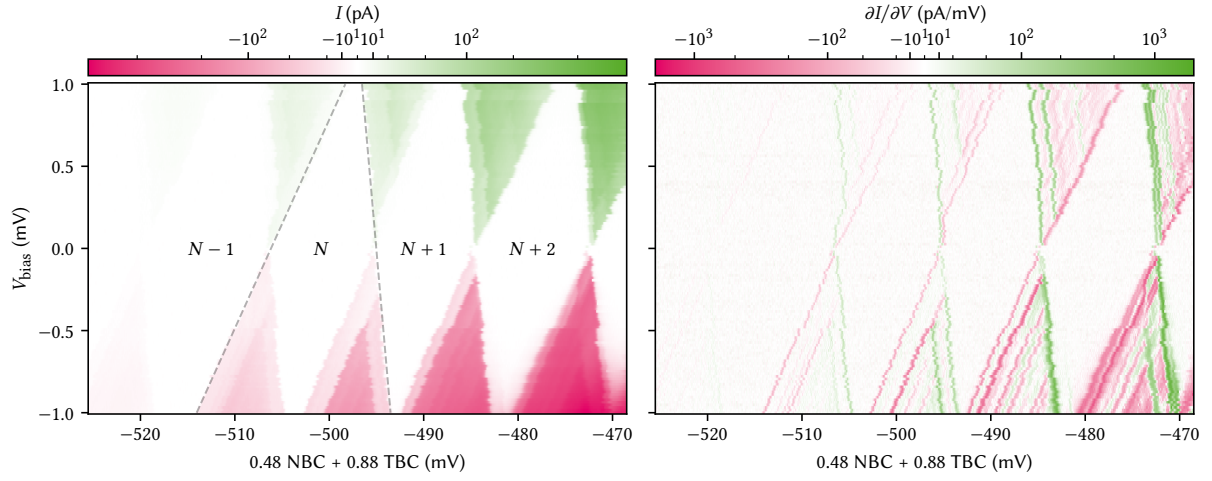


Figure 6.1

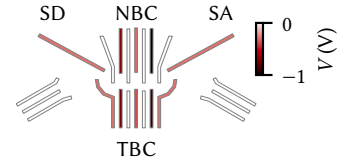


Figure 6.2

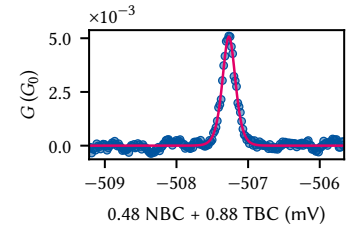


Figure 6.3

Characterization and improvements of the optical path

7



Vibration performance

A microscope's performance is limited chiefly by two factors; first and foremost the resolution and imaging fidelity are limited by the systematic aberrations introduced by the optics.¹ Various types of aberrations exist, and modern microscopes usually include a complex assembly of optics to compensate for these errors. The second factor is vibration noise. This becomes more significant the higher the resolution of the microscope simply because ambient, environmental vibrations within the range of human civilization is typically on the order of $100\text{ }\mu\text{m/s}$ root mean square (RMS) [1]. Comparing that to transmission electron microscopes (TEMs) with atomic resolution, it is clear that these instruments require purpose-built rooms to reduce the vibration level to acceptable levels.

The demands on the microscope discussed in the present thesis are fortunately much more relaxed as the features we need to resolve are on the micrometer scale. However, we face the additional challenge of ultra-low temperatures, or rather the manner in which they are achieved. The microscope is integrated into a *dry* dilution refrigerator (DR). In contrast to a *wet* DR, which uses a liquid Helium bath, these systems achieve the pre-cooling necessary for the $^3\text{He}/^4\text{He}$ dilution refrigeration cycle to work by adding a secondary refrigeration mechanism, a pulse tube refrigerator (PTR). These are closed-cycle systems that work with ^4He compressed to ~ 21 bar on the high-pressure and ~ 7 bar on the low-pressure side. A rotating valve connecting high and low pressure lines to the cryostat in turn produces alternating gas flow inside a regenerator, where the gas absorbs heat at the low-temperature and deposits heat at the high-temperature end [2, 3]. In commercial PTRs the frequency of the pulses of Helium gas, determined by the rotary valve motor, is usually fixed at values around 1.5 Hz.

Naturally, the compressor, the rotary valve motor, and the Helium pulses themselves introduce vibrations into the cryostat. While the cold foot of the PTR is not rigidly connected to the cryostat interior,² the entire cold head assembly rests with rubber feet on the cryostat top plate in the system's delivery status. Thus, our microscope does not only encounter passive environmental vibrations but also the active disturbance from the PTR.

This chapter is laid out as follows. In Section 8.1, I briefly discuss the theoretical underpinnings of vibration isolation to inform its optimization. To characterize and improve upon the isolation, I performed vibration noise spectroscopy using the techniques and tools presented in Part I. I employed two different approaches that I lay out in the following; first, using a commercial piezoelectric accelerometer (Section 8.2) and second, using the optical response of a spatial reflectance gradient (Section 8.3). As will become clear, the two approaches complement each other because they are sensitive to slightly different quantities.

8.1 Vibration isolation

A simple yet effective method of vibration isolation is to suspend the system on passive air springs. These are typically constructed with two

1: Besides the limit set by the wavelength-dependent diffraction, of course.

2: In the Oxford Instruments Triton 450 copper braids connect the cold head to the first pulse tube stage (PT1) and second pulse tube stage (PT2) plates. There exist commercial systems that use gas exchange instead, for example the CryoConcept HEXA-DRY series [4].

separate air chambers, a spring and a damping chamber, connected by pneumatic tubing. The load is rigidly mounted to a plunger that rests on a diaphragm sealing the spring chamber. Excitations of the load induce oscillations in the variable spring chamber volume. The connection to the fixed-volume damping chamber provides a flow impedance³ that manifests as a damping force to the spring chamber oscillations.

Let us adopt a simple toy model to gain an intuition for the behavior of a mass suspended on air springs as function of vibration frequency by modelling it as a damped harmonic oscillator. We can compute the transfer function $H(s)$ for external perturbations $u(t)$ from the Laplace transform of the Newtonian equation of motion

$$\ddot{x}(t) + 2\gamma\dot{x}(t) + \omega_0^2 x(t) = m^{-1}u(t) \quad (8.1)$$

for the displacement from equilibrium $x(t)$. Here, γ is the damping constant, ω_0 the resonance frequency of the undamped system, and m the oscillator mass. The amplitude transfer function given by

$$H(s) = \frac{x(s)}{u(s)} = \frac{1}{m} \frac{1}{s^2 + 2\gamma s + \omega_0^2} \quad (8.2)$$

is drawn in Figure 8.1 normalized to the DC response for $s = i\omega$ (solid black line). Below $\omega = \sqrt{2}\omega_0$ (vertical dotted line), the suspension in fact leads to amplification of external impulses. This is independent of the damping γ and the reason why resonance frequencies as small as possible are desirable in vibration isolation. Above this frequency, the system attenuates with 40 dB per decade. A more accurate model results in the transfer function drawn as a dashed line [5]. Here, the attenuation at high frequencies is only 20 dB per decade.

From Figure 8.1, we can infer two possible approaches to isolating a mass from vibrations. The first is to make the system's resonance frequency ω_0 as small as possible by resting it on a spring damping system. This maximizes the region in which external influences are attenuated. The second is to do the opposite, *i.e.*, make the entire system as stiff and thereby ω_0 as large as possible.⁴ While this minimizes the attenuation region, it also moves the amplification region close to the resonance to higher frequencies, and possibly further away from the external excitation. Consequently, this approach makes most sense if it is known that low-frequency excitations are the dominant source of vibrations.

What does this mean for our case of a dry DR? The rotary valve motor of the PTR generates pulses with frequency 1.4 Hz. Commercial damping systems that the space constraints in our lab allow to be accommodated, for example the CFM Schiller MAS 25 [6], have resonance frequencies around $f_0 = 2.5$ Hz, implying the first two harmonics of the PTR excitation fall into the amplification regime as discussed above. We are thus right in-between the two regimes and it is a-priori unclear which isolation scheme to choose without detailed mechanics simulations. Hence, the initial isolation concept for the cryostat envisaged mounting the rotary valve motor rigidly to the stiff aluminium item profile frame, which was additionally filled with sand to increase the system's resonance frequency.

However, prompted by a sudden increase in visually observed vibrations in the microscope image, I modified the cryostat frame to house three air springs [6] in the hopes of isolating the microscope from external disturbances.⁵ To this end, I decoupled the frame from which the cryostat itself is suspended from the support frame standing on the lab ground. Extruding from the square footprint of the support frame at two adjacent

3: The speed of a fluid in laminar flow through a round pipe is proportional to the pressure gradient along the flow direction and to the square of the distance from the wall.

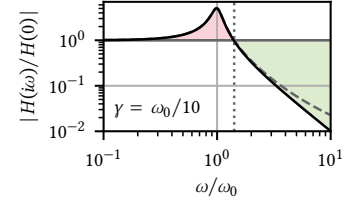


Figure 8.1: Force transmission function of a damped harmonic oscillator (solid black line). Below $\omega = \sqrt{2}\omega_0$ (dotted vertical line), external excitations are amplified (shaded red area). For larger damping γ , the amplification at resonance becomes smaller (not shown). Above $\omega = \sqrt{2}\omega_0$, excitations are attenuated (shaded green area). The dashed line shows a more realistic model for an air spring [5], whose attenuation above the break frequency becomes smaller as the damping constant γ is increased, whereas the harmonic oscillator's high-frequency behavior is independent of γ .

[5]: (n.d.), *Vibration Damping with Low-Frequency Air Springs*

4: The stiffness k is related to the resonance frequency by $k = m\omega_0^2$.

[6]: CFM Schiller GmbH (n.d.), *Type MAS*

5: As it turned out, the cause was a damaged nanopositioner bearing rather than environmental. Fortunately, the endeavour still proved successful and resulted in an improved vibration performance as I show below.

corners and the center of the diametrically opposite side, the three air springs are mounted with the base on angle brackets connected to the support frame while their plunger is mounted to a second angle bracket connected to the cryostat frame. The springs are connected by pneumatic tubing to a central pressure regulation panel that is connected to the building's central air pressure line. The vertical placement of the springs is chosen such that when the air springs are deflated the cryostat frame rests on the support frame, establishing the same rigid connection that existed previously. This allows examining the influence of the air springs on the vibration isolation without modifying the setup by simply venting the pressurized air from the springs.

In the following, I will characterize the performance of the system with and without the air springs active using two different methods.

8.2 Accelerometric vibration spectroscopy

The most straightforward method of measuring vibration noise is an accelerometer. These are devices that convert translational forces, for example by means of a loaded spring, into electrical signals. They are mounted rigidly to the device under test (DUT) and typically connected to some sort of signal conditioner providing a constant current bias to the sensor and putting out a voltage proportional to the acceleration. The most sensitive and low-frequency designs use piezoelectric materials like Quartz crystals for sensitivities in the range of 10 V/g with a broadband noise floor of 2 μ g [7].

To assess the vibration level in the sample position, I designed a small angle bracket onto which the accelerometer⁶ can be screwed either in vertical or horizontal direction in the sample puck of the DR, allowing measurements of the displacement noise along the direction of gravity as well as perpendicular to it and the optical axis. The accelerometer is connected to the coaxial cables installed in the cryostat via an adapter cable from 10-32 to SubMiniature version A (SMA) connector. Outside of the cryostat, the signal is routed to a signal conditioner that provides the necessary current bias and outputs a voltage which is digitized by a Keysight 34465A digital multimeter (DMM) connected to the measurement computer.

Since the sensor's (conditioned) output is a voltage directly proportional to the acceleration, it is straightforward to compute the displacement PSD from time series data measured with the DMM using the `python_spectrometer` package presented in Chapter 3 [8]. Leveraging the `fourier_procfn` argument, I transformed the voltage data first to acceleration and then, by integration, to displacement in frequency space as indicated in Listing 8.1. To assess the impact of the PTR and the suspension, I measured the displacement noise PSD for each combination of the two being switched on and off. The cryostat was closed, its vacuum chamber evacuated, and the magnet, a significant seismic mass, mounted as usual. The measurements are shown in Figure 8.2 together with the band-limited RMS (cf. Equation 2.14),

$$\text{RMS}_S(f) = \sqrt{\int_{f_{\min}}^f df' S^2(f')}. \quad (8.3)$$

[7]: (n.d.), 731-207 *Compact Seismic Accelerometer*, 10 V/g

6: Wilcoxon 731-207 kindly lent by Marcus Eßer [7].

```
from qutil.signal_processing
    ↳ import fourier_space
from qutil.functools import
    ↳ chain, scaled
from qutil import const

sensitivity = scaled(1 / 9.9 /
    ↳ const.g)
fourier_procfn = chain(
    sensitivity,
    fourier_space.derivative
)
```

Listing 8.1: Functionality to transform the conditioned voltage to displacement in Fourier space.

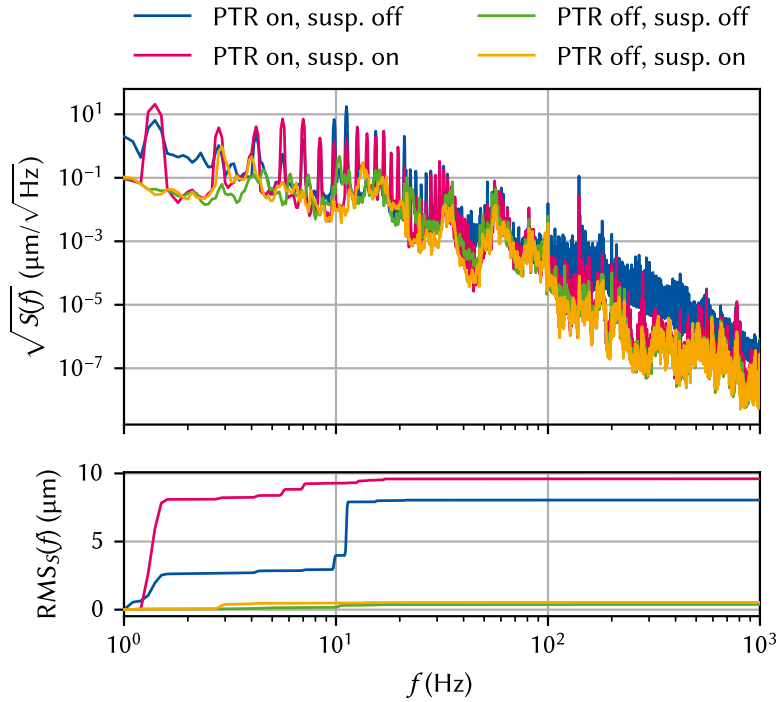


Figure 8.2: Top: displacement noise spectra acquired with the accelerometer at room temperature when the PTR is switched on (blue, magenta) or off (green and orange), and when the air suspension is switched enabled (magenta, orange) or disabled (blue, green). Bottom: band-limited RMS computed from the power spectral densities (PSDs) in the upper panel (cf. Equation 2.14). Turning on the PTR increases the RMS noise amplitude by more than an order of magnitude over the entire frequency spectrum. The suspension slightly worsens the total noise because the low-frequency pulses excite the system close to the air springs' resonance frequency of 2.5 Hz.

When the PTR is switched off, the spectra with and without suspension are dominated by broadband vibration noise, although quite some structure around 15 Hz, 33 Hz and 60 Hz can be observed.⁷ When it is switched on, the PTR pulses at 1.4 Hz and a large number of its higher harmonics visually dominate the spectra. Clearly, the suspension has a larger impact in this case, matching qualitatively the behavior discussed in Section 8.1. At high frequencies, it manages to almost completely suppress the broadband excitation observed without the suspension. At low frequencies, on the other hand, the PTR harmonics are amplified to the degree that the band-limited RMS is dominated by their contribution. Only at around 10 Hz, the attenuation starts to take effect. Overall, the PTR is found to raise the displacement noise amplitude from 0.5 μm RMS to 10 μm RMS, while the suspension, over the entire frequency range, has at best no positive influence.

This result is less than encouraging. At that level of RMS-fluctuations, we'd have a slim chance of resolving micrometer-scale features using the microscope. But is the *absolute* magnitude of displacement noise at the sample position really the correct measure for the microscope performance? Indeed, if the sample oscillates in phase with the objective and ocular lenses as well as the single-mode fiber (SMF), we will still obtain a perfect imaging fidelity. So actually only the *relative* displacements of sample, lenses, and detection fiber affect the microscope's performance. To characterize these, I developed an optical *in-situ* technique to measure the displacement noise based on knife-edge reflectance fluctuations that I will present in the following section.

8.3 Optical vibration spectroscopy

The gate electrodes on our samples are fabricated using two separate lithography processes; first, the smallest structures are written using

7: Note the curious peaks slightly offset from the second and third harmonic of the PTR frequency in the spectrum with suspension enabled and PTR disabled. We may speculate that these are due to the PTRs of other cryostats in other labs in the vicinity that are transmitted through the floor. Two were running two rooms over at the time the data was acquired.

electron-beam lithography (EBL) in two steps. Then, larger structures on the order of $1\text{ }\mu\text{m}$ and above are written using optical lithography. In the region where the two overlap on the mesa to establish electrical contact, the highly reflective Ti/Au optical gates have a width of $14\text{ }\mu\text{m}$ and a height of 160 nm and lie on top of the poorly reflecting GaAs surface, resulting in a step-like reflectance profile. Scanning perpendicularly across such a straight edge between a poorly and a highly reflecting material is known as a knife-edge measurement and is typically used to measure the spatial extent of a laser spot [9–11]. We can use the same setup to measure the displacement noise; instead of manually shifting our knife edge across the beam spot, though, we measure the reflectance fluctuations induced by the knife edge fluctuating relative to the spot.

The scenario is sketched in Figure 8.3 in the coordinate system defined by the magnet such that z is along gravity's axis and x is the out-of-plane axis. Focusing the laser (indicated by a dashed circle) onto the edge of the optical gate, we can move the sample using the y -axis nanopositioner and observe a decrease in reflected intensity if the gate is moved away from the laser and an increase if it is moved towards the laser. This gradient in reflected intensity can be inverted to obtain the vibration noise along y by monitoring the intensity as a function of time.

Let us take a closer look at the reflected intensity when the laser spot has a finite overlap with the edge of the gate. Under the simplifying assumption of a perfectly sharp drop-off and taking the reflectance of the gold gate to be unity, we can write the reflectance as function of the coordinate perpendicular to the gate edge at $y = 0$ as

$$R(y) = \begin{cases} 1, & y \leq 0 \\ r, & y > 0, \end{cases} \quad (8.4)$$

where r is the reflectance of the bare GaAs surface. Assuming a perfect Gaussian (transverse electric (TEM)₀₀ mode) beam characterized by its waist radius w_0 at which the intensity drops to $1/e^2$ of its maximum value, the laser intensity profile in 1D is given by

$$I(y) = I_0 \exp\left(-\frac{2y^2}{w_0^2}\right), \quad (8.5)$$

where $I_0 = P_0/w_0$ with P_0 the total beam power. The power reflected when the spot partially overlaps with the reflectance step can then be expressed as the convolution

$$P_R(y) = R(y) * I(y) \quad (8.6)$$

$$= \frac{I_0 w_0}{2} \sqrt{\frac{\pi}{2}} \left[1 - (1-r) \operatorname{erf}\left(\frac{y\sqrt{2}}{w_0}\right) \right] \quad (8.7)$$

in the yz focal plane, where $\operatorname{erf}(y)$ is the error function.

The function is plotted in Figure 8.4. The contrast that can be achieved is given by $1-r$. Furthermore, for $y \in [-w_0/2, w_0/2]$ the function is well-approximated by

$$P_R(y) \approx -I_0(1-r)y + \frac{I_0 w_0}{2} \sqrt{\frac{\pi}{2}} \quad (8.8)$$

drawn as a dashed line. Since we measure the photon count rate rather than the power, $\Phi = P\lambda/hc$ with λ the laser wavelength, we rewrite this

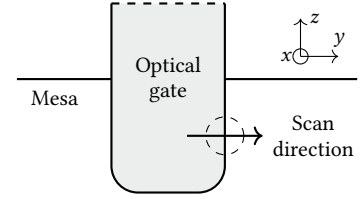


Figure 8.3: Sketch of the region of the sample used for optical vibration spectroscopy. The coordinate system follows the magnet's; z is parallel to gravity, and x is perpendicular to the quantum well (QW) plane. The optical gate extends further north as indicated by the dashed line.

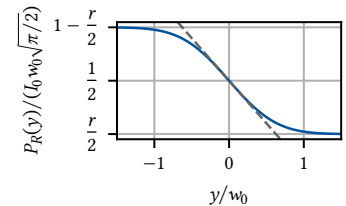


Figure 8.4: Theoretical reflected power for a Gaussian beam of width w_0 and a reflectance contrast of $1-r$ according to Equation 8.6. The dashed line indicates the leading order approximation at $y = 0$.

as

$$\Phi_R(y) = -sy + \frac{\Phi_0}{2} \sqrt{\frac{\pi}{2}}. \quad (8.9)$$

where we defined the *sensitivity*

$$s = \frac{\Phi_0}{w_0} (1 - r). \quad (8.10)$$

Hence, to obtain a more sensitive probe for vibrations, meaning that small variations in y lead to large variations in Φ_R , one could either improve the reflectance contrast $1 - r$, decrease the spot size w_0 , or increase the incident photon flux Φ_0 .⁸ In our case, the former two are fixed by the setup and sample, whereas the latter is limited by the maximum data transfer rate of the Swabian Instruments Time Tagger 20 counting card, 9 MS/s.

Starting from Equation 8.9, it is straightforward to obtain the displacement in the vicinity of $y = 0$ as function of photon flux,

$$y(\Phi_R) = \frac{w_0}{1 - r} \left[\frac{1}{2} \sqrt{\frac{\pi}{2}} - \frac{\Phi_R}{\Phi_0} \right]. \quad (8.11)$$

To summarize, we can position the laser spot on the edge of an optical gate and record a time trace of the photon flux by using the Time Tagger to count the photons detected by the avalanche photodiodes (APDs) mounted on the side exit of the spectrometer. Using Equation 8.11 we can then convert the flux into a displacement and proceed with the usual spectral noise estimation as explained in Part I.

I will now lay out the experimental procedure of calibrating the system to (implicitly) obtain the parameters w_0 , r , and Φ_0 . The first challenge is obtaining a proper length reference scale. While the nanopositioners on which the sample is mounted do in principle have a resistive position readout, it is extremely unreliable at small displacements. Therefore, I calibrated the relative position using the imaging arm of the optical head. Figure 8.5 depicts the procedure. I illuminated the sample with the white light, positioned the spot on the edge of the optical gate, and imaged the sample with the Thorlabs DCC1545M complementary metal-oxide-semiconductor (CMOS) camera. I then extracted the position of the edge, in pixels, for several rows to obtain some statistics by fitting a linear function to the edge profile in a small region between two refraction maxima. Repeating this step for different DC voltages applied to the nanopositioner, this yields the proportionality factor between the nanopositioner DC voltage, V_{DC} , and the position of the gate edge on the camera. By measuring the total width of the gate on the camera image, I obtained the magnification by referencing it to the design width,

$$M = \frac{w[\text{px}]}{w[\mu\text{m}]}. \quad (8.12)$$

Again performing a linear fit (shown in the upper panel of Figure 8.6) to the data for different voltages then results in the linear transformation from DC voltage to position.

Finally, I switched from white light illumination to the laser, focused it onto the edge of a gate, and measured the photon count rate reflected off the sample as a function of V_{DC} , from which we can finally extract the desired sensitivity (slope) $s \approx 2.36(2)$ Mcps/ μm of count rate over displacement. The data and fit are shown in the bottom panel of Figure 8.6. Clearly, the count rate is linear in the displacement over a large range,

8: Note that the smaller w_0 , the smaller also the maximum displacement amplitude that can be resolved as the derivative goes to zero as $y \rightarrow \pm\infty$.

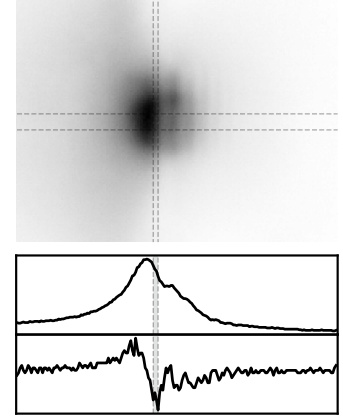
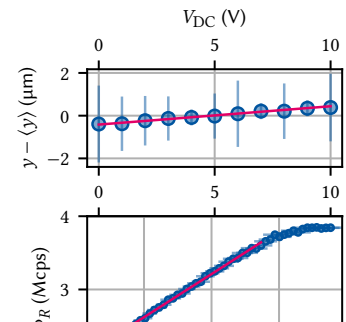


Figure 8.5: Calibration of the length reference scale. The top shows a CMOS camera image (higher intensity darker) of the white light spot on the edge of the optical gate as indicated in Figure 8.3. Several diffraction lines can be seen parallel to the edge. The vertical dashed lines indicate the region in which the intensity slope was fitted. The horizontal dashed lines indicate the extent of rows averaged over. The lower plots show a line cut along the central row of the considered region (top) and its derivative (bottom).



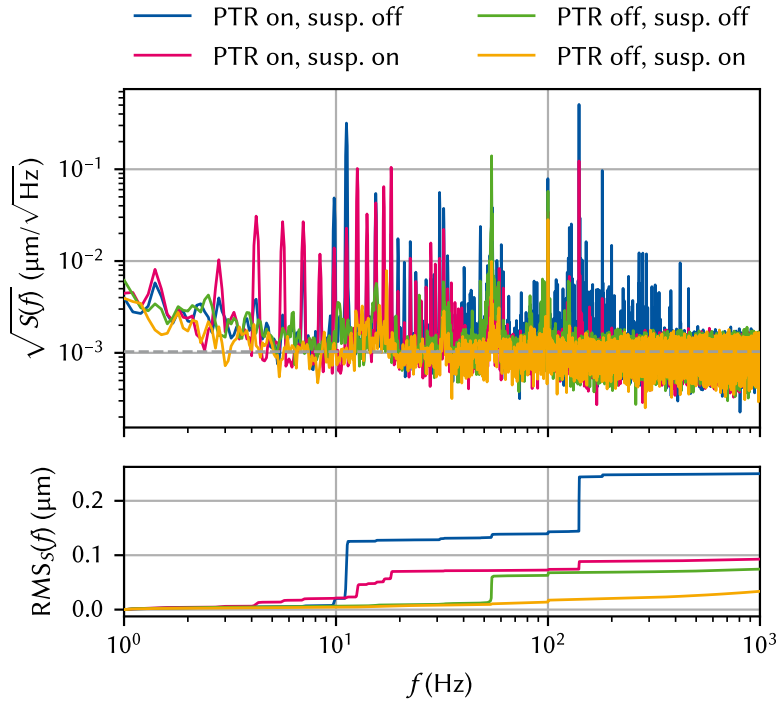


Figure 8.7: Top: displacement noise spectra acquired with the optical *in-situ* method at room temperature when the PTR is switched on (blue, magenta) or off (green and orange), and when the air suspension is switched enabled (magenta, orange) or disabled (blue, green). The dashed gray line indicates the theoretical noise floor derived in Subsection 8.3.1. Bottom: band-limited RMS computed from the PSDs in the upper panel (cf. Equation 2.14). The PTR has a much smaller effect than when measuring the absolute displacement noise with the accelerometer, increasing the RMS only by a factor of two. While the lowest-order PTR harmonics are amplified by up to an order of magnitude in amplitude with the suspension enabled, they contribute relatively little to the total RMS and are compensated by the superior high-frequency attenuation behavior. The total $\text{RMS}_S \approx 100$ nm in working mode is below the typical μm feature size.

indicating that for fluctuations with amplitude on the order of 100 nm RMS, the measurement sensitivity should be sufficiently robust.

We are now at last able to measure the displacement noise using `python_spectrometer`. Setting `procfn` to the linear transformation given in Equation 8.11 and measuring the counts registered by the APDs using the Time Tagger,⁹ I obtained the displacement noise PSDs shown in Figure 8.7. A few things stand out. First, rather than the f^{-2} background observed with the accelerometer in Section 8.2, the noise floor is white ($S(f) = \text{const.}$) at approximately $1 \text{ nm}/\sqrt{\text{Hz}}$. To understand why, we need to take a closer look at the counting statistics, which we will postpone for a bit in order to first finish our discussion of the noise spectra. Second, the overall noise level is much – by a factor of 20 RMS – lower than with the accelerometer. We can attribute this to the fact that the optical method is sensitive to relative rather than absolute displacements. If the cryostat and the optical head were infinitely stiff we would measure no displacement noise with this method – intrinsic noise floor notwithstanding – whereas the accelerometer is still sensitive to oscillations of the cryostat on the air spring fulcrum. In that sense the optical method gives us the more pertinent results because only the displacements “experienced” by the light travelling through the microscope ultimately matter. Third, in contrast to the accelerometer measurements, the RMS amplitude is reduced by half when the suspension is active. Although the harmonics of the PTR frequency of 1.4 Hz are again amplified by the suspension below 10 Hz, raising the band-limited RMS above that with the suspension disabled, there occurs a crossover at the eighth harmonic frequency beyond which the attenuation outweighs the amplification at low frequency.¹⁰

8.3.1 Noise floor

The noise floor in the optical vibration measurements shown in Figure 8.7 is qualitatively very different from that observed with the accelerometer.

9: Since the APDs are arranged in a Hanbury Brown-Twiss (HBT) geometry, I combined the counts of both instruments using the virtual channel functionality of the Time Tagger.

10: It furthermore appears that even a measurement whose sole electronic device is a picosecond-resolution counting card cannot escape 50 Hz power line noise (or in this case its second harmonic).

There, the *acceleration* noise floor was white,¹¹ whereas with the optical method the *displacement* noise floor is white, hinting at a different underlying mechanism.

To elucidate this issue, we model the detection event of a single photon (a “click”) arriving at the detector at a random time t_i as a δ -function so that the total flux as function of time is given by

$$\Phi(t) = \sum_i \delta(t - t_i). \quad (8.13)$$

Assuming them to be uncorrelated, the time difference between subsequent clicks is exponentially distributed with average rate $\bar{\Phi}$, $|t_{i+1} - t_i| \sim \text{Exp}(\bar{\Phi})$ [12]. From this it follows that the number of clicks $N(\Delta t)$ within a given time bin $t \in [s, u]$ of length $\Delta t = |u - s|$ is Poisson distributed, $N(\Delta t) \sim \text{Pois}(\bar{N})$, with mean number of counts $\langle N(\Delta t) \rangle = \bar{N} = \bar{\Phi} \Delta t$ [13]. Using the formalism developed in Section 2.1, we can now compute the PSD of the stochastic process $\delta N(\Delta t) = N(\Delta t) - \bar{N}$. To this end, observe that because we assumed arrivals to be uncorrelated, $N_{u'}(\Delta t)$ for a time bin starting at $t = u'$ is independent of $N_{s'}(\Delta t)$ for a time bin starting at $t = s'$. In other words, the autocorrelation function of $\delta N(\Delta t)$ is nonzero only for the same time bins,

$$C_{\delta N(\Delta t)}(\tau) = \langle (N_s(\Delta t) - \bar{N})(N_u(\Delta t) - \bar{N}) \rangle = \text{Var}(N(\Delta t))\delta(\tau), \quad (8.14)$$

where $\tau = s' - u'$ and $\delta(\tau)$ is to be understood in a broad sense as zero if $|\tau| > \Delta t$ and $1/2\Delta t$ else. For the Poisson distribution the variance is equal to its mean so that we obtain

$$C_{\delta N(\Delta t)}(\tau) = \bar{N}\delta(\tau). \quad (8.15)$$

In the limit of $\Delta t \rightarrow 0$, we can then perform the Fourier transform to obtain the PSD of $\delta N = \lim_{\Delta t \rightarrow 0} \delta N(\Delta t)$,¹²

$$S_{\delta N}(\omega) = \bar{N}, \quad (8.16)$$

that is, δN is a white noise without frequency dependence.¹³ $S_{\delta N}$ can be seen as the *instantaneous* number noise PSD.

As a last step, we consider once again discretely sampling the *continuous* process δN with PSD $S_{\delta N}(\omega)$ at rate $f_s = \Delta t^{-1}$ in order to find an expression for the PSD of the discrete process $\delta N(\Delta t)$, $S_{\delta N(\Delta t)}(\omega)$. We know from above that $\text{Var}(\delta N(\Delta t)) = \bar{N}$. On the other hand, recall from Section 2.1 that also

$$\text{Var}(\delta N(\Delta t)) = \int_{-\infty}^{\infty} \frac{d\omega}{2\pi} S_{\delta N(\Delta t)}(\omega) = \int_{-f_s/2}^{f_s/2} df S_{\delta N(\Delta t)}(f) \quad (8.17)$$

where the last equation holds true because of the finite bandwidth of the discretely sampled signal. Since $S_{\delta N}$ is white, it follows that $S_{\delta N(\Delta t)}$ is, too, and we can directly evaluate Equation 8.17, obtaining¹⁴

$$S_{\delta N(\Delta t)}(\omega) = \frac{\bar{N}}{f_s}. \quad (8.18)$$

To convert to the displacement noise PSD, we can simply convert units using the calibration derived above because if $N \sim \text{Pois}(\bar{N})$ then so $y \sim \text{Pois}(\bar{N}f_s/a)$ where a is the slope of the calibration converting displacements to count rates (Figure 8.6). Hence,¹⁵

11: Remember that as acceleration is the second time derivative of displacement, in frequency space it is proportional to f^2 times the latter.

12: Despite appearances, $S_{\delta N}$ has units cts^2/Hz . The discrepancy stems from the difficulty in defining a continuous white noise process.

13: Note that we could have also arrived at this result directly by computing the autocorrelation function $\langle \delta N(t)\delta N(t - \tau) \rangle$ from Equation 8.13 with $N(t) = \int dt \Phi(t)$.

14: $S_{\delta N(\Delta t)}$ also has units cts^2/Hz .

15: Note that this is the two-sided PSD; to convert to the one-sided version used in this chapter, multiply by two.

$$S_{\delta y(\Delta t)}(\omega) = \frac{\bar{N}}{f_s} \times \left(\frac{f_s}{a} \right)^2 = \frac{\bar{\Phi}}{a^2} \quad (8.19)$$

with $\delta y = y - \langle y \rangle$. This type of noise is known as *shot noise*. It was first studied in the context of electron transport by Schottky [14] and results from the discrete nature of, in our case, photons and their stochastic emission times [15]. For the parameters in the present measurements, $\bar{\Phi} \approx 3$ Mcps and $s \approx 2.36$ Mcps/ μm (cf. Figure 8.6), we obtain a shot noise floor of $S_{\delta y(\Delta t)} \approx 1 \text{ nm}/\sqrt{\text{Hz}}$ in excellent agreement with the data shown in Figure 8.7 where the theoretical value is indicated by a grey dashed line.

8.4 Routes for improvement

Several improvements could be made to the system if the external conditions would allow it. First, the rotary valve motor should be moved further away from the cold head.¹⁶ As per the initial installation status, it is currently connected to the cold head with a flexible hose at a right angle and a distance of roughly 50 cm, which is below the minimum bend radius recommended by Oxford Instruments.¹⁷ Additionally, the term “flexible” is relative here given the pressure of 20 bar. Increasing the length of the hose should reduce its relative rigidity and thereby its ability to transmit vibrations from the motor to the cold head.

Next, the cold head should be mounted firmly to a secondary reference frame, for instance the ceiling or the lower cryostat frame on which the springs rest. An intuitively obvious step, it has also been shown in the literature that decoupling the PTR from the cryostat in this fashion leads to significant improvements in vibration isolation [16].¹⁸ Acoustic insulation of the room and PTR flex hoses could further improve the low-frequency response of the system [17, 18]. Lastly, let me note that there also exist cryocoolers with variable operating frequency that can thus be tuned away from problematic resonances in the system [19].

In Appendix A, I show additional spectroscopy data, including data measured along the gravitational axis in the puck and on the floor of different rooms, which suggests moving to a different laboratory could also benefit the vibration stability, as well as data for different configurations of the PTR motor.

[20, 21]

16: Clearly, this will impact the performance of the PTR to some extent and should therefore be considered carefully.

17: Note that the orientation of the motor, which is horizontal with the axis, is also not the recommended configuration.

18: The former option was attempted, but showed no clear improvements in the measurements for reasons unclear, see Appendix A for additional data. It did emphatically deteriorate the inter-departmental atmosphere. Apologies to the institute on the floor above.

Conclusion & outlook

9



Part III

**OPTICAL MEASUREMENTS OF
ELECTROSTATIC EXCITON TRAPS IN
SEMICONDUCTOR MEMBRANES**

Part IV

A FILTER-FUNCTION FORMALISM FOR UNITAL QUANTUM OPERATIONS

APPENDIX

Additional vibration spectroscopy data



Bibliography

- [1] Colin G. Gordon. “Generic Vibration Criteria for Vibration-Sensitive Equipment.” In: *Optomech. Eng. Vib. Control*. Optomechanical Engineering and Vibration Control. Vol. 3786. SPIE, Sept. 28, 1999, pp. 22–33. DOI: [10.1117/12.363802](https://doi.org/10.1117/12.363802). (Visited on 10/14/2022) (cited on page 28).
- [2] Ray Radebaugh. “Cryocoolers: The State of the Art and Recent Developments.” In: *J. Phys.: Condens. Matter* 21.16 (Mar. 2009), p. 164219. DOI: [10.1088/0953-8984/21/16/164219](https://doi.org/10.1088/0953-8984/21/16/164219). (Visited on 05/01/2025) (cited on page 28).
- [3] A. T. A. M. de Waele. “Basic Operation of Cryocoolers and Related Thermal Machines.” In: *J Low Temp Phys* 164.5 (Sept. 1, 2011), pp. 179–236. DOI: [10.1007/s10909-011-0373-x](https://doi.org/10.1007/s10909-011-0373-x). (Visited on 05/01/2025) (cited on page 28).
- [4] 1-HEXA-DRY M. Cryoconcept. URL: <https://cryoconcept.com/product/hexa-dry-m/> (visited on 05/02/2025) (cited on page 28).
- [5] *Vibration Damping with Low-Frequency Air Springs*. Fabreeka. URL: <https://www.fabreeka.com/wp-content/uploads/2025/04/Fabreeka%20Low%20Frequency%20Pneumatic-2019-EN.pdf> (visited on 05/02/2025) (cited on page 29).
- [6] CFM Schiller GmbH. *Type MAS*. URL: <https://www.cfm-schiller.de/en/vibration-isolation-technology/products/luftfedern/type-mas/> (visited on 05/02/2025) (cited on page 29).
- [7] *731-207 Compact Seismic Accelerometer, 10 V/g*. Wilcoxon Sensing Technologies. URL: <https://wilcoxon.com/731-207/> (visited on 05/02/2025) (cited on page 30).
- [8] Tobias Hangleiter et al., *Python-Spectrometer* version 2024.11.1, Nov. 21, 2024. Zenodo. DOI: [10.5281/ZENODO.13789861](https://doi.org/10.5281/ZENODO.13789861) (cited on page 30).
- [9] J. A. Arnaud et al. “Technique for Fast Measurement of Gaussian Laser Beam Parameters.” In: *Appl. Opt.*, AO 10.12 (Dec. 1, 1971), pp. 2775–2776. DOI: [10.1364/AO.10.002775](https://doi.org/10.1364/AO.10.002775). (Visited on 05/05/2025) (cited on page 32).
- [10] D. R. Skinner and R. E. Whitcher. “Measurement of the Radius of a High-Power Laser Beam near the Focus of a Lens.” In: *J. Phys. E: Sci. Instrum.* 5.3 (Mar. 1972), p. 237. DOI: [10.1088/0022-3735/5/3/015](https://doi.org/10.1088/0022-3735/5/3/015). (Visited on 05/05/2025) (cited on page 32).
- [11] John M. Khosroffian and Bruce A. Garetz. “Measurement of a Gaussian Laser Beam Diameter through the Direct Inversion of Knife-Edge Data.” In: *Appl. Opt.*, AO 22.21 (Nov. 1, 1983), pp. 3406–3410. DOI: [10.1364/AO.22.003406](https://doi.org/10.1364/AO.22.003406). (Visited on 05/05/2025) (cited on page 32).
- [12] *Exponential Distribution*. In: *Wikipedia*. Apr. 15, 2025. (Visited on 05/07/2025) (cited on page 35).
- [13] *Poisson Distribution*. In: *Wikipedia*. Apr. 26, 2025. (Visited on 05/07/2025) (cited on page 35).
- [14] W. Schottky. “Über spontane Stromschwankungen in verschiedenen Elektrizitätsleitern.” In: *Annalen der Physik* 362.23 (Jan. 1918), pp. 541–567. DOI: [10.1002/andp.19183622304](https://doi.org/10.1002/andp.19183622304). (Visited on 05/07/2025) (cited on page 36).
- [15] Ya. M. Blanter and M. Büttiker. “Shot Noise in Mesoscopic Conductors.” In: *Physics Reports* 336.1 (Sept. 1, 2000), pp. 1–166. DOI: [10.1016/S0370-1573\(99\)00123-4](https://doi.org/10.1016/S0370-1573(99)00123-4). (Visited on 05/06/2025) (cited on page 36).
- [16] E. Olivieri et al. “Vibrations on Pulse Tube Based Dry Dilution Refrigerators for Low Noise Measurements.” In: *Nuclear Instruments and Methods in Physics Research Section A: Accelerators, Spectrometers, Detectors and Associated Equipment* 858 (June 2017), pp. 73–79. DOI: [10.1016/j.nima.2017.03.045](https://doi.org/10.1016/j.nima.2017.03.045). (Visited on 08/15/2022) (cited on page 36).
- [17] D. Schmoranzner et al. “Cryogenic Broadband Vibration Measurement on a Cryogen-Free Dilution Refrigerator.” In: *Cryogenics* 98 (Mar. 1, 2019), pp. 102–106. DOI: [10.1016/j.cryogenics.2019.01.010](https://doi.org/10.1016/j.cryogenics.2019.01.010). (Visited on 05/02/2022) (cited on page 36).
- [18] Seong Woo Oh et al. “Cryogen-Free Scanning Gate Microscope for the Characterization of Si/Si_{0.7}Ge_{0.3} Quantum Devices at Milli-Kelvin Temperatures.” In: *AIP Advances* 11.12 (Dec. 21, 2021), p. 125122. DOI: [10.1063/5.0056648](https://doi.org/10.1063/5.0056648). (Visited on 05/02/2025) (cited on page 36).

- [19] *Two Stage Pulse Tubes*. TransMIT. URL: <https://cryo.transmit.de/en/products/two-stage-pulse-tubes> (visited on 05/05/2025) (cited on page 36).
- [20] S. Caparrelli et al. "Vibration-Free Cryostat for Low-Noise Applications of a Pulse Tube Cryocooler." In: *Review of Scientific Instruments* 77.9 (Sept. 19, 2006), p. 095102. DOI: [10.1063/1.2349609](https://doi.org/10.1063/1.2349609). (Visited on 05/02/2025) (cited on page 36).
- [21] M. Pelliccione et al. "Design of a Scanning Gate Microscope for Mesoscopic Electron Systems in a Cryogen-Free Dilution Refrigerator." In: *Review of Scientific Instruments* 84.3 (Mar. 12, 2013), p. 033703. DOI: [10.1063/1.4794767](https://doi.org/10.1063/1.4794767). (Visited on 05/02/2025) (cited on page 36).

Special Terms

A

APD avalanche photodiode. 33, 34

C

CMOS complementary metal-oxide-semiconductor. 33

D

DMM digital multimeter. 30

DR dilution refrigerator. 28–30

DUT device under test. 30

E

EBL electron-beam lithography. 32

H

HBT Hanbury Brown-Twiss. 34

P

PSD power spectral density. iii, 30, 31, 34, 35

PT1 first pulse tube stage. 28

PT2 second pulse tube stage. 28

PTR pulse tube refrigerator. 28–31, 34, 36

Q

QW quantum well. 32

R

RMS root mean square. 28, 30, 31, 34

S

SMA SubMiniature version A. 30

SMF single-mode fiber. 31

T

TEM transmission electron microscope. 28, 32